Meteorol Atmos Phys (2018) 130:473–484
https://doi.org/10.1007/s00703-017-0535-8

ORIGINAL PAPER

Temporal and spatial analysis of precipitation patterns in an Andean region of southern Ecuador using LAWR weather radar

Fernando Oñate-Valdivieso[1] · Andreas Fries[1] · Katherine Mendoza[1] · Victor Gonzalez-Jaramillo[1] · Franz Pucha-Cofrep[1] · Rütger Rollenbeck[2] · Jörg Bendix[2]

Received: 8 September 2016 / Accepted: 17 May 2017 / Published online: 26 May 2017

Abstract This paper focuses on the analysis of precipitation patterns, using a Local Area Weather Radar to collect information about the precipitation distribution in an Andean region of southern Ecuador (cities of Loja, Zamora and Catamayo). 54 representative events were selected to develop daily precipitation maps and to obtain their relevant characteristics, which were related to the topography and the season. The results showed that a strong correlation between the areas covered by precipitation (R_A coefficient) and the season exists. In general, humid air masses come from the east (Amazon Basin), but during the main rainy season (December to April), humidity also frequently enters the study region from the west (Pacific Ocean). The rainy season is characterized by convective precipitation, associated with higher evaporation rates during austral summer. The relatively dry season is formed between May and November, but considerable precipitation amounts are registered, too, due to advective moisture transport from the Amazon Basin, a result of the predominant tropical easterlies carrying the humidity up the eastern escarpment of the Andes, generally following the natural course of the drainage systems.

Responsible Editor: C. Simmer.

✉ Fernando Oñate-Valdivieso
fronate@utpl.edu.ec

[1] Departamento de Geología, Minas e Ingeniería Civil (DGMIC), Hidrología y Climatología Working Group, Universidad Técnica Particular de Loja, Loja, Ecuador

[2] Laboratory for Climatology and Remote Sensing (LCRS), Faculty of Geography, University of Marburg, Marburg, Germany

1 Introduction

The knowledge of the spatiotemporal distribution and dynamics of rainfalls in the tropical Andes remains insufficient, due to the spare operational meteorological station network (e.g., Barry 2008). Furthermore, the complex topography makes reliable estimation of the spatiotemporal precipitation distribution highly challenging (Gabella and Notarpietro 2004; Germann et al. 2006, 2009; Villarini and Krajewski 2010). Nevertheless, precipitation data from meteorological stations have been widely used to investigate rainfall formation processes even in complex terrain (e.g., Espinoza et al. 2015), although this information has great uncertainties, including measurement errors, especially in windy environments and exposed positions (Rollenbeck and Bendix 2006). However, rain gauge measurements facilitate point data accurately (Jensen and Pedersen 2005), but these data must be extrapolated to obtain areawide precipitation maps to analyze the rainfall distribution. The accuracy of these maps depends highly on the density of the existing station network, because climate conditions change considerably within short distances, especially in the Andes of southern Ecuador (Rollenbeck and Bendix 2011; Fries et al. 2014).

In general, the rainfall distribution and amounts in mountain areas depend on the atmospheric flow and the local topography, because the mountain ridges act as barriers and modify the spatial and temporal rainfall distribution (e.g., Johansson and Chen 2005). Furthermore, the precipitation distribution is linked to the stability conditions, wind speed, perpendicularity of the flow to the terrain, and the height of the mountain ridges (Foresti and Pozdnoukhov 2012). Under unstable conditions (convective cloud formation), the rainfall distribution depends on whether the convection is thermally induced or caused by

mechanical lifting over the level of free convection. If the atmospheric flow is thermally induced, the highest precipitation amounts are observed at the mountain tops, because the diurnal mountain–valley–breeze affects the rainfall distribution; if the convection is forced orographically (mechanical lifting), the precipitation is enhanced on the windward side of the mountain, because the mountain chains force the air to uplift, the water vapor condenses, and heavy rainfall is produced on the upwind slope (Panziera and Germann 2010; Fries et al. 2014). Under stable conditions (advective moisture transport), the rainfall distribution depends on whether the atmospheric flow is blocked or unblocked. Blocked conditions mean that the wind flow is not directly perpendicular to the mountain chain, which causes an air flow around the mountain barrier, shifting the humidity further upstream, where the highest precipitation amounts are observed. Unblocked conditions indicate a wind flow perpendicular to the mountain chain. When wind speed is high, the air flows directly over the ridge, enhancing precipitation on the lower windward slope and decreasing with height as well as towards the interior of the mountain chain (e.g., Houze et al. 2001). Therefore, a spare meteorological station network in tropical mountains can hardly detect the real rainfall distribution even if advanced statistical interpolation methods are applied.

Weather radar systems are an alternative, because they can capture the spatiotemporal rainfall distribution in high resolution over large areas (Krajewski et al. 2011; Lengfeld et al. 2014). By means of the radar data, the complexity of the precipitation distribution and the rainfall forming processes can be evaluated more precisely (Rollenbeck and Bendix 2011; Fries et al. 2014). In general, weather radars measure the precipitation indirectly, quantifying the echo of the electromagnetic waves that are reflected by the falling raindrops (Jensen and Pedersen 2005). However, like rain gauges, weather radars have deficiencies, especially in mountainous regions, because higher mountain tops cause beam blockage and clutter fields, leaving little or no information for the affected areas (e.g., Germann and Joss 2004; Pedersen et al. 2010). Therefore, several methods were developed to overcome these problems, e.g., blending the radar information with rain gauge data from the surface (e.g., Delrieu et al. 2014; Bendix et al. 2017). As Rollenbeck and Bendix (2011) as well as Fries et al. (2014) showed in their studies, the combination of rain gauge data and radar observations is reliable to determine the spatiotemporal rainfall distribution and its variations even in high mountain areas, such as the southern Andes of Ecuador.

The conventional weather radars of the national weather services in developed countries generally use S-band and C-band technology, due to their more sophisticated capabilities, including three-dimensional scans and Doppler technology (e.g., Bell et al. 2015). Nevertheless, due to their wider range, their application is limited in mountain areas, because the radar beam increases height with greater distances from the emitter, which is caused by the earth curvature, and therefore, precipitation cannot be detected in the whole radar coverage (rainfall occurs under the radar beam in areas further away from the emitter; Pedersen et al. 2010). X-band radars lack these more sophisticated capabilities and must be calibrated by means of rain gauge data at the surface; however, due to their shorter range, the operation in mountain areas is more advantageous, not to mention the lower investment costs of this radar type (Jensen 2002; Bendix et al. 2017).

Using the information from an X-band radar (Local Area Weather Radar (LAWR); Jensen 2002), it is possible to analyze the precipitation patterns inside an Andean mountain catchment in southern Ecuador, to obtain the relevant characteristics of precipitation, related to the topography and the season.

2 Materials and methods

2.1 Study area

The study area is located in the Andes of southern Ecuador between the coordinates 3°42′S/79°12′W and 4°15′S/78°49′W within an altitudinal range between 840 and 3760 m (Fig. 1). The orientation of the Andes (north–south), which are divided into various mountain ridges in southern Ecuador, causes a very complex topography, generating strong variation in climate over short distances (Rollenbeck and Bendix 2011).

The climate in the study area is characterized by strong altitudinal gradients in air temperature, air humidity, and rainfall (e.g., Bendix et al. 2009; Fries et al. 2009, 2012). The predominant wind direction is from the east because of the tropical easterlies (Emck 2007), which carry the humidity from the Amazon Basin up the eastern escarpment of the Andes. However, due to the north–south orientation of the Andean mountain ridges, the humidity transport from the Amazon Basin is impeded, because the individual mountain ridges act as barriers (Fries et al. 2014).

In the study area, northeast winds prevail between January and April, while southeast winds dominate between April and October. From June to September, the wind direction rarely changes and the highest wind speeds are observed (monthly average of 15.5 m s^{-1}; Windhorst et al. 2013). With the beginning of austral summer (October/November), the tropical easterlies weaken and the wind direction becomes more variable, but the proportion of easterly winds is still over 50%. During austral summer (December to April), the easterly winds are frequently

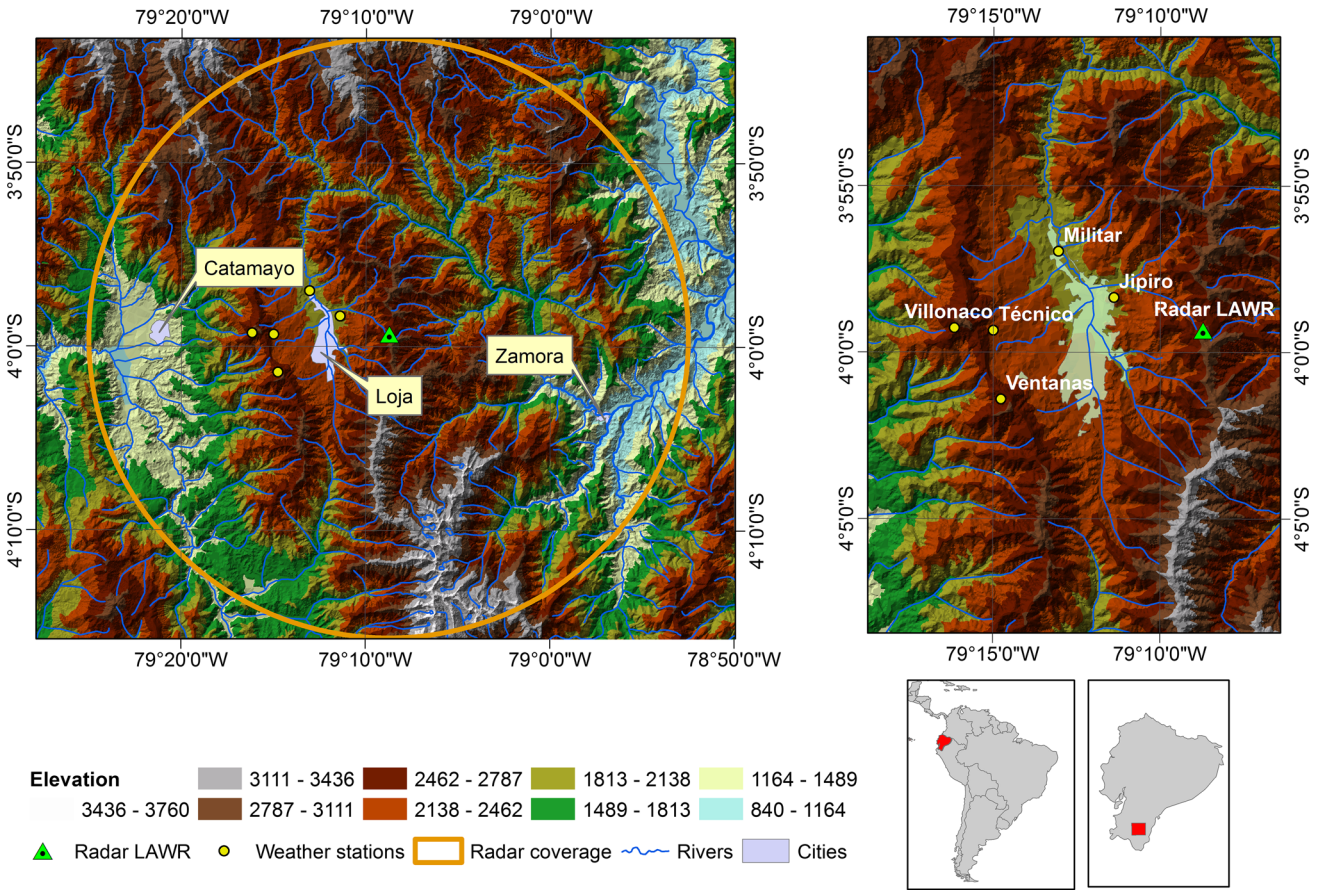

Fig. 1 Study area

interrupted by short periods of westerly winds from the Pacific, which generally brings dry and sunny weather to the study area, because the air masses lose their moisture content at the western escarpment of the Andes (Rollenbeck and Bendix 2011). However, during this period, the formation of convective storms is very common, especially in the inter-Andean basins such as in the valleys of Loja and Catamayo, provoking the main rainy season for this region (Vuille et al. 2000; Fries et al. 2014).

The valley of Loja is characterized by a per-humid climate, where low mountain forests, pastures, and crops dominate, due to the enhanced population pressure (Ochoa-Cueva et al. 2015). The valley of Catamayo in the west is relatively dry and naturally covered by the xerotropical vegetation; however, the predominate crops are sugar cane (*Saccharum officinarum*) and maize (*Zea mays*; Ochoa-Cueva et al. 2016).

2.2 Existing weather stations

The location of the existing meteorological stations in the study area is represented in Fig. 1. The stations are Davis Wireless Vantage Pro2^{TM} Plus, composed of a set of instruments that include a rain collector, temperature and humidity sensor, solar radiation senor as well as wind speed and direction. The stations provide weather information with a temporal resolution of 10 min. The technical specifications of the meteorological stations can be found in the Davis Instruments Manual (2015).

2.3 The Local Area Weather Radar (LAWR)

The Local Area Weather Radar (LAWR) is a meteorological radar based on X-band technology and is installed on top of the El Tiro mountain (3°59′S/79°8′W) at an elevation of 2850 m, approximately 3 km from the center of the city of Loja. In some sectors (west and south), the radar signal is obstructed by higher mountains, but the LAWR covers 97% of the area within its maximum range of 60 km (radius).

The LAWR is based on the marine radar FURUNO 1525 Mk. III with an output power of 25 kW. The transmission frequency is 9410 ± 30 MHz with a bandwidth of 3 MHz and a pulse length of 1.2 ms at a repetition rate of 600 Hz. The antenna uses a slotted waveguide as an emitter and is 2.80 m long. The radar scans at a single elevation

with a horizontal beam width of 0.95° and a vertical beam width of 10° (up and down). The antenna rotates at 24 rpm, performing 120 scans in 5 min, which are merged with the final images (LAWR Documentation, Jensen 2004). The radar generates three images every 5 min with different ranges (60, 30, and 15 km) and resolutions (500 m × 500 m, 250 m × 250 m, and 100 m × 100 m). For this study, the 100 m × 100 m images were used, because for hydrological investigations, the highest resolution is always desired.

2.4 Generation of daily precipitation maps

2.4.1 Radar images correction

First, the LAWR raw images are corrected for the decay of the radar signal with the distance from the emission source, using an empirical exponential function based on auxiliary data from satellite cloud analysis (Bendix et al. 2004). The exponential function is modified according to the wear output of the magnetron, changing the function parameters over time (Rollenbeck and Bendix 2006). Then, relief obstacles that cause beam shadows are determined by means of a DEM and the affected image sections corrected by amplifying the signal in relation to the remaining beam volume. After this, a mask file is derived from the raw images to determine all clutter fields (areas without information due to the terrain obstacles, signal errors, etc.). The method for detecting clutters for the high-resolution images was improved by adjusting the thresholds (Fries et al. 2014), because the images with a resolution of 100 m × 100 m show high variable clutter fields. The clutter variability is mainly caused by the different surface reflectivity during and after rain events when soil moisture content is changing, but also by a slight instability of the antenna tower (movements caused by wind). The detected clutters are subtracted from the raw radar image and all the affected pixels are set to zero. Then, the clutter fields are interpolated bilinearly by means of the values from their margins to fill the gaps with estimated values (Rollenbeck and Bendix 2011). Finally, the corrected raw images (every 5 min) are added up to generate daily images.

2.4.2 Radar image calibration

The daily radar images were calibrated by means of rainfall measurements from the meteorological stations at the surface. Therefore, the daily measured station data were interpolated, applying ordinary kriging, to generate an areawide precipitation map with the same resolution as the radar images (100 m × 100 m). Then, the interpolated station data at each pixel was related to the radar reflectivity value for the same grid cell, where a meteorological station exists. The obtained relation values were interpolated, applying ordinary kriging, to generate a relation surface with the same resolution as the radar image. Ordinary kriging was used, because the station distribution in the study area reflects the topography very well. Finally, the radar images were calibrated by means of the relation surface to obtain the precipitation quantity at each pixel for the whole study area (Fries et al. 2014).

To guaranty the reliability of the precipitation amounts and their distribution, a weighting map was generated, derived from the spatial and altitudinal location of the weather stations. The area of influence of each station's data was determined by its horizontal and vertical location within the study area. Based on this map, the calibrated radar data and the station data were merged, giving the station data a weight of one at its precise location and then changing slightly over to the calibrated radar values with increasing distance from the station (blending; Fries et al. 2014). To estimate the accuracy of the method, a cross validation was applied (Germann et al. 2009).

Daily precipitation maps were generated exclusively for the valley of Loja, located in the center of the study area, because all available station data are concentrated there, which is indispensable for reliable radar image calibration (see Fig. 1).

2.5 Analysis of precipitation patterns

From the LAWR database, 54 storms were selected, which showed precipitation totals higher than 10 mm in 24 h (10 mm day^{-1}), corresponding to the years 2013, 2014, and 2015 (Table 1). Storms with less precipitation were not considered, except for those recorded in September, because this is the driest month in the core study area and precipitation events generally do not reach such magnitudes.

To analyze the spatial rainfall distribution, the daily precipitation maps were generated by means of the methodology described in Sect. 2.4, using GIS. The spatial distribution of the selected precipitation events is uneven due to the presence of the Andean mountain ridges, which cross the study area from the north to the south, forming barriers, and the prevailing wind direction during the individual rainfall event (Jensen and Pedersen 2005; Fries et al. 2014). Based on the calibrated daily precipitation maps, the area covered by precipitation (ha) was calculated, divided into the following categories: ≤10, >10 to ≤20, >20 to ≤30, >30 to ≤40, >40 to ≤75, and >75 mm day^{-1}. The rain-area coefficient (R_A) was proposed to relate the area of precipitation of the categories greater than 10 mm day^{-1} [$A_{>10}$ (ha)] to the total area covered by the storm [A_T (ha)]. The coefficient R_A would classify the storms analyzed based on the area with higher levels of precipitation. The equation is written as follows:

Table 1 Storms parameters

Date (dd/mm/yyyy)	Area (mm day^{-1})						R_A	M_R (mm day^{-1})	Predominant paths
	≤10 (ha)	>10 (ha)	>20 (ha)	>30 (ha)	>40 (ha)	>75 (ha)			
10/01/2014	33,862.5	7293.75					0.18	15.44	West, southwest
10/01/2015	35,850	5268.75	12.5				0.13	21.68	East
18/01/2015	14,806.25	23,625	2718.75				0.64	23.66	Southeast, east
27/01/2015	2250	18,181.3	19,275	1412.5	25		0.95	42.91	Northeast
05/02/2014	27,237.5	13,912.5					0.34	18.02	West
07/02/2015	13,862.5	9275.0	14,025.0	3918.8	68.8		0.66	48.23	Southwest, west
08/02/2015	23,150	18,000					0.44	19.79	West, northwest
10/02/2015	35,950	4262.5	937.5				0.13	27.52	West, southwest
01/03/2014	1089.6	12,785.6	15,156.4	10,903.8	1103.9		0.97	48.86	Northeast
02/03/2014	15,849.0	17,476.1	7562.1	8.0			0.61	30.48	West
03/03/2014	19,612.5	16,656.3	4868.8	12.5			0.52	30.46	West, south
04/03/2014	25,412.5	12,518.8	2606.3	593.8	18.8		0.38	41.60	South
05/03/2014	16,113.0	24,799.9					0.61	19.32	Northeast
08/03/2014	25,399.0	15,765.0					0.38	18.49	Southeast, northeast
09/03/2014	8749.7	18,738.4	11,966.8	1440.5			0.79	39.98	Northwest, northeast
16/03/2014	20,495.2	16,658.4	3761.1	57.7			0.50	31.59	Northeast
31/03/2014	19,312.5	21,825.0					0.53	20.16	Northeast
18/03/2015	0.0	615.6	2509.8	8160.1	29,316.1	473.6	1.00	77.00	Southeast, northeast
26/03/2015	9.0	1137.4	9383.9	17,014.9	13,580.2	4.0	1.00	75.30	Northeast, west
17/04/2015	40,943.75	206.25					0.01	11.72	Northeast, southwest
25/04/2015	24,475	16,625	50				0.41	20.98	Southeast, northeast
26/04/2015	30,256.25	10,887.5					0.26	15.83	Southeast, northeast
30/05/2013	17,380.5	23,449.0	180.3				0.58	23.31	East
31/05/2013	98.8	9631.3	25,922.3	5401.2			1.00	38.51	East
08/05/2014	25,298.6	12,267.1	3265.4	170.6			0.38	32.06	Northeast
09/05/2014	15,157.8	11,167.1	8642.9	6077.9			0.63	40.13	Southwest
12/05/2014	2526.8	38,447.7	31.3				0.94	21.06	East
23/05/2014	20,190.7	20,826.1					0.51	18.90	Northeast
30/06/2013	17,253.1	23,760.8					0.58	17.34	East, northeast
01/06/2014	37,232.0	3810.7					0.09	16.78	Northeast
13/06/2014	30,167.9	10,935.3					0.27	18.56	East, northeast
14/06/2014	24,902.8	16,168.4					0.39	16.70	Southeast, east
15/06/2014	27,118.8	13,980.2					0.34	17.55	Southeast, east
08/07/2013	26,346.5	14,756.6					0.36	18.24	East
07/07/2014	28,799.9	12,333.1					0.30	19.26	Southeast, east
08/07/2014	34,437.5	6706.3					0.16	12.00	East
09/08/2014	37,268.8	3868.8					0.09	13.62	East
13/08/2014	21,606.3	19,531.3					0.47	20.98	East, southeast
23/09/2013	34,611.4	6519.3	26.8				0.16	22.94	East, northeast
29/09/2013	41,137.5						0.00	9.8	East, southeast
12/09/2014	41,137.5						0.00	3.82	Northeast, southeast
09/10/2014	7766.3	28,838.8	4386.1				0.81	27.79	Southeast
10/10/2014	17,953.6	22,741.0	257.3				0.56	24.80	Southeast
11/10/2014	10,117.7	27,663.2	3170.7	4.0			0.75	30.75	Southeast
25/10/2014	22,431.3	15,375.0	3337.5				0.45	22.74	Southwest
26/10/2014	41,101.2	4.0					0.00	10.08	South, southwest
01/11/2014	31,325.0	9731.3	62.5	18.8			0.24	33.52	Northeast, southeast, west

Table 1 continued

Date (dd/mm/yyyy)	Area (mm day^{-1})						R_A	M_R (mm day^{-1})	Predominant paths
	≤10 (ha)	>10 (ha)	>20 (ha)	>30 (ha)	>40 (ha)	>75 (ha)			
05/11/2014	39,115.6	1870.2	126.2				0.05	22.42	Southeast, southwest
10/11/2014	22,330.6	18,665.9					0.46	18.69	Southeast
11/11/2014	33,519.4	7368.1					0.18	13.28	Southwest
18/11/2014	16,136.4	7972.1	12,352.5	4564.8			0.61	36.30	Northeast, northwest, west
08/12/2014	33,326.2	7630.8	175.9				0.19	26.71	West, southwest
09/12/2014	19,385.8	15,126.2	6152.1	352.7			0.53	32.31	West
11/12/2014	40,975.0	156.3					0.00	10.59	Northwest

$$R_A = \frac{A_{>10}}{A_T}. \quad (1)$$

In addition, the maximum daily rainfall amount [M_R (mm day^{-1})] as well as the predominant wind direction (storm path) of each selected event in the core study area was calculated. The storm trajectory of each event was determined by means of the radar images. Therefore, the position of the centroid of the storm was identified and then the hourly spatial offset determined during the whole rainfall event (see Fig. 5). The identified trajectories were overlaid with a digital elevation model to observe their interaction with the relief. Likewise, the relationship between the trajectories and the season was analyzed. Furthermore, the extreme values of R_A, the average rainfall amount, and the predominant storm path of all individual events were calculated for each month and related to the annual season.

3 Results and discussion

Figure 2 presents seasonal variation in rainfall. The main rainy season in the inter-Andean valleys is formed between December and April, while August and September are the driest months (Rollenbeck and Bendix 2011; INAMHI 2009). A marked difference between wet and dry season is observed in the valley of Catamayo, because the mountain chains to the east inhibit the humidity transport form the Amazon Basin. However, the valley of Loja receives considerable precipitation amounts even during the dry season, because only one mountain ridge separates the valley from the Amazon Basin and humidity can be transported into the valley (Fig. 2a). Nevertheless, precipitation amounts are lower compared to the rainy season, because rainfall generally occurs in the form of long lasting drizzle (Fries et al. 2014). Further to the east, at the eastern escarpment of the Andes, a different annual cycle can be observed. At altitudes over 1000 m, the main rainy season is formed between May and September, due to the higher wind speeds during these months, making the humidity transport from the Amazon Basin more effective (Windhorst et al. 2013). The relative dry season occurs between November and February, because wind speed is lower and the general wind flow from the east is frequently interrupted by westerly wind from the Pacific. The city of Zamora, located in the transition zone between the eastern escarpment of the Andes and the Amazon Basin, shows the typical tropical cycle with abundant rainfall throughout the year and peaks in March/April and October (Fig. 2b), associated with the movement of the intertropical convergence zone (Richter 2003; Fries et al. 2014). Figure 3

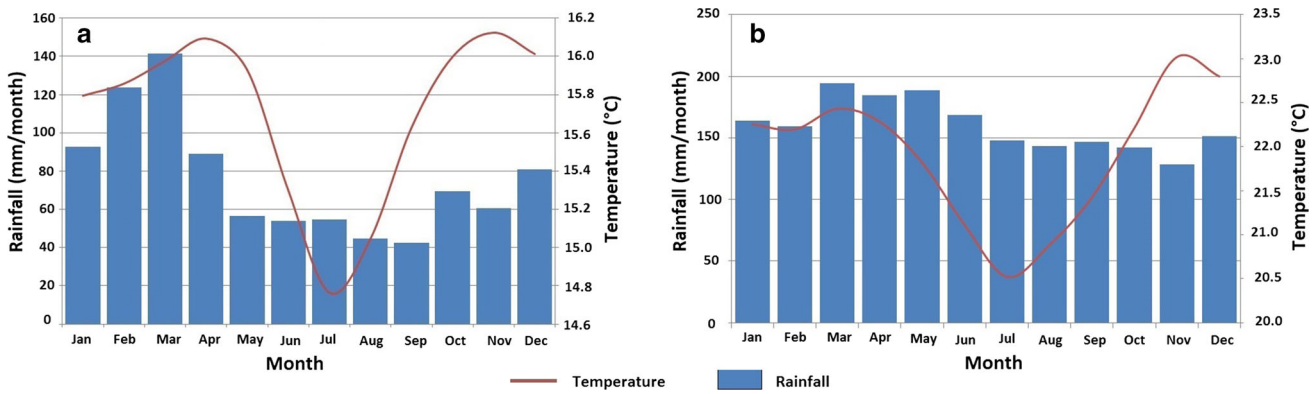

Fig. 2 Seasonal variation in rainfall: **a** City of Loja (station La Argelia, period 1965–2014). **b** City of Zamora (station Zamora, period 1965–2014)

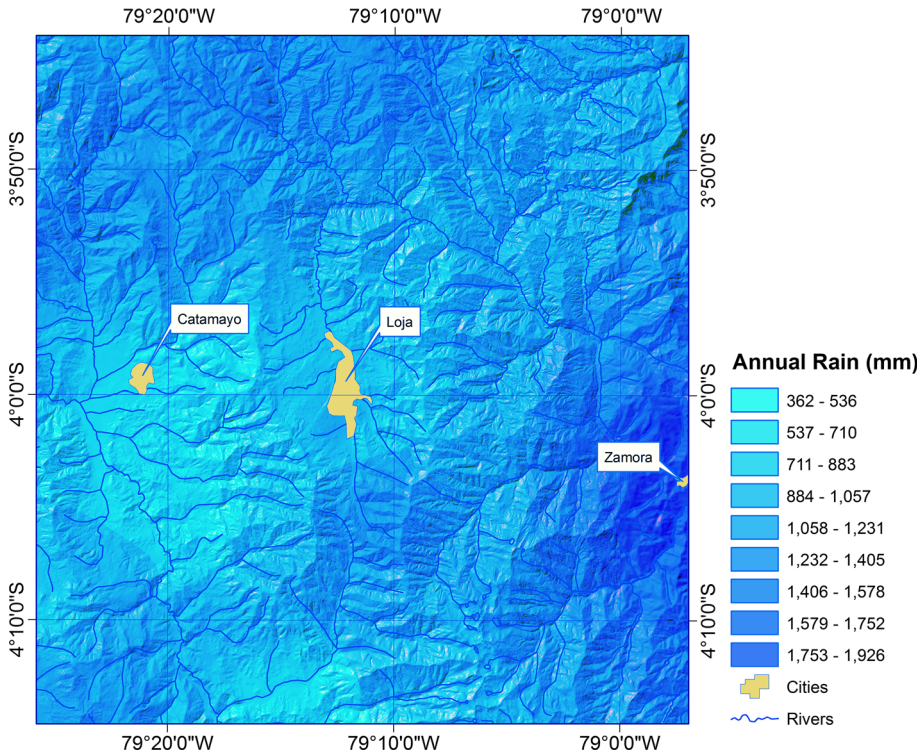

Fig. 3 Total annual precipitation in the study area

presents an annual precipitation map of the study area, drawn up with the data recorded from the meteorological station network of the Ecuadorian Weather Service (Instituto Nacional de Meteorología e Hidrología [INAMHI] INAMHI 2009). The strong horizontal gradients in precipitation amounts are clearly visible; within a distance of 30 km the climate conditions change from semiarid, with an average annual precipitation of 354 mm (valley of Catamayo), to humid, with an average annual precipitation of 2297 mm (city of Zamora, eastern escarpment of the Andes; Bendix et al. 2009). In summary, the study region comprises the humid eastern escarpment of the south Ecuadorian Andes, covered by tropical rain forests (up to an altitude of about 1800 m), tropical cloud forests at higher elevations, and paramo (above 3000 m; Richter 2003; Rollenbeck and Bendix 2006).

Table 1 presents the results for the selected 54 precipitation events. It is clearly visible that extreme rainfall events with areawide daily precipitation quantities over 30 mm day^{-1} occur during the rainy season in austral summer (between December and April). This is due to the enhanced evapotranspiration during this period, which frequently causes the formation of convective thunderstorms; for which reason, the highest daily precipitation amounts are observed. In the dry season (between May and October), areawide precipitation quantities are notably lower (generally below 20 mm day^{-1}), especially between June and September. During these months, dominant wind direction is from the east and the advective moisture transport from the Amazon Basin is more effective, due to the higher wind speeds (Windhorst et al. 2013). However, the eastern mountain ridge of the core study area forms a barrier for easterly wind flows, which impedes the humidity transport into the valley, and therefore, rainfall amounts are lower.

To illustrate the influence of topography and wind direction on the precipitation distribution (Foresti and Pozdnoukhov 2012), four specific rainfall events were selected (Fig. 4), which summarize the atmospheric conditions and the variability in rainfall distribution during the different annual seasons. In general, the precipitation amounts vary between 0 and 75 mm and the rainfall is distributed unevenly over the study area, depending on the predominant wind direction during a specific precipitation event as well as the orientation and altitude of the mountain ridges.

The daily precipitation map for the event on May 31, 2013 displays precipitation amounts up to 40 mm (Table 1). The highest precipitation amounts were observed at the upper part of the eastern mountain ridge while further to the west rainfall decreases. During this day, wind direction was from the east and the humidity was transported from the Amazon Basin up the eastern escarpment of the Andes. The wind direction is perpendicular to the eastern mountain ridge and unblocked conditions can be stated (Fig. 1), which means that the highest precipitation amounts occur on the lower windward slope of the barrier, decreasing with height and towards the west.

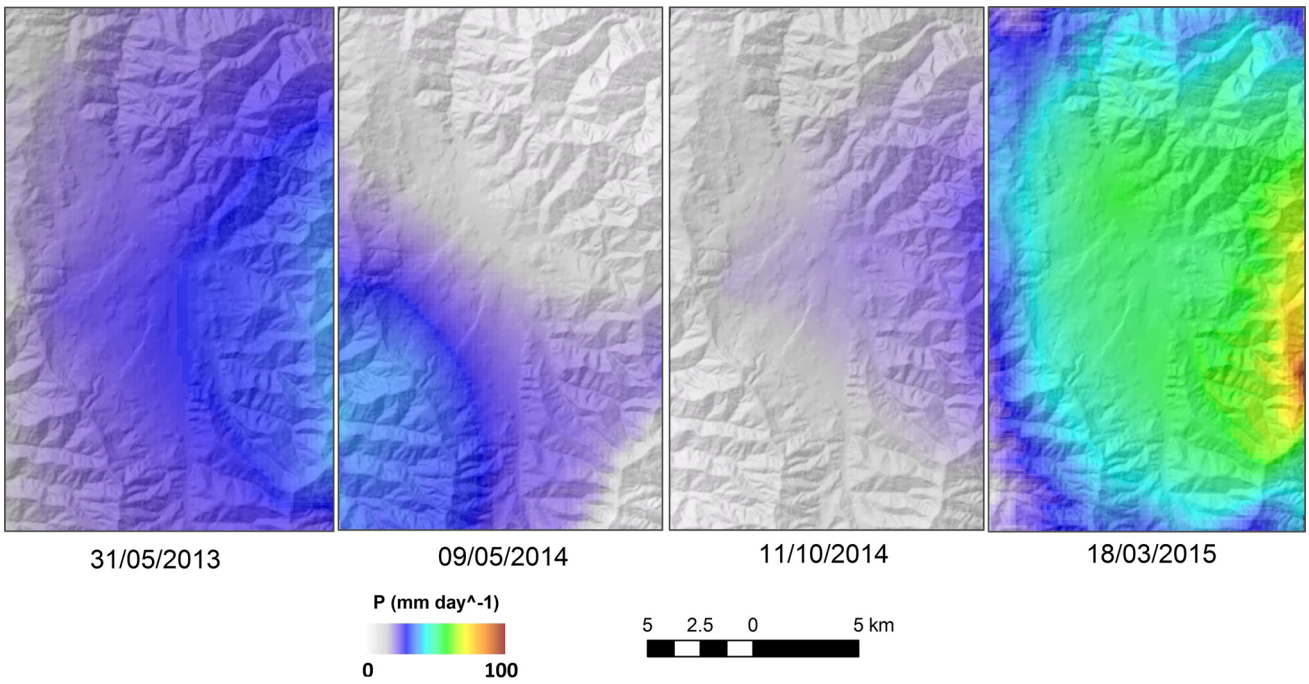

Fig. 4 Selected daily precipitation maps

After the ridge rainfall decreases, because most of the humidity has previously precipitated, the lee effect causes the dissolving of the clouds due to the descending air.

On May 9, 2014, general wind direction was from the southwest (Table 1) and precipitation amounts reached 40 mm, concentrated at the southwestern mountain ridge. Due to the relatively small area covered by rainfall, a convective event in the neighboring valley of Catamayo can be fixed. The highest precipitation amounts are displayed on the upwind slope, because convection was forced orographically. Afterwards, the southwestern barrier precipitation decreased quickly, because the uplifting air lost the majority of its humidity content during the ascent. Only where the top altitude of the southwestern mountain ridges is lower, small amounts of humidity could enter the valley of Loja and were transported to the eastern mountain ridge, due to the prevailing southwestern wind direction.

Wind direction during the event on October 11, 2014 was from the southeast (Table 1), but precipitation amounts did not exceed 25 mm. The rainfall is concentrated at the eastern mountain ridge, forming a barrier for humidity transport under these atmospheric conditions. The southeastern mountain ridge has the highest top altitudes of the whole study area, and therefore, only small amounts of precipitation could enter the valley of Loja. However, the southeastern barrier changes its orientation from north–south to north–east further to the north (Fig. 1), which cause the wind direction to be perpendicular to the ridge and stable unblocked conditions can be assumed for this portion of the barrier. The highest rainfall amounts are displayed on the top of the eastern barrier, but most of the humidity had precipitated before, and therefore, rainfall amounts remained low for the whole core study area.

During the event of March 18, 2015, easterly wind directions were dominant and rainfall total exceeded 75 mm. The extremely high rainfall totals covered the entire valley of Loja, because the varying northeasterly to southeasterly wind flow allowed the confluence of the humidity close to the eastern mountain ridge (Fig. 1). Such high precipitation amounts are unusual for the study area, for which the storm caused the overflow of various rivers and triggered several landslides in different parts of the valley (El Comercio 2015; Ecuavisa 2015). This extreme event can be explained by means of the high evaporation rates over the Amazon Basin, which is due to the perpendicular sun position during this month. However, the eastern mountain ridge forms a barrier, but wind direction was not perpendicular to the mountain ridges, which provokes stable blocked conditions and the humidity is transported towards the drainage systems into the interior of the mountain chain. Nevertheless, the eastern mountain ridge of the core study area impedes the moisture transport into the valley under easterly flow conditions, but, due to the extremely high humidity content of the air, a huge moisture amount could reach the valley, although precipitation amounts might be even higher on the windward slopes of the eastern barrier.

The established R_A coefficient (Table 1) relates the area covered by rainfall above 10 mm with the total area of the storm and serves as an indicator for the magnitude and type

of the storm. Convective precipitation generally produces intense rains over small-to-moderate areas, and therefore, the R_A coefficient should be high for these events (between 0.5 and 1). Advective precipitation covers greater parts of the surface, but rainfall intensity is lower, and therefore, R_A coefficient values are lower (between 0 and 0.5).

As expected, in the study area, convective storms occur predominantly during the rainy season in austral summer when temperatures are higher (Fig. 2). In the colder months, during austral winter, a stratiform (advective moisture transport) precipitation is dominant. This is confirmed by the maximum daily rainfall amounts (M_R, Table 1), where the highest daily precipitation totals are recorded during austral summer (max. 77 mm; May 2015) and minimum values during austral winter (min. 3.8 mm; September 2014), which also can be related to the annual seasons (rainy season and dry season).

Table 2 summarizes the R_A coefficients and M_R of the individual storm for the respective month. The highest values of R_A and M_R occur between December and April, which correspond to the main rainy season. May is an exception, but this month must be considered as a transition month to the dry season. This is also indicated in Table 1, because a convective storm occurs until the middle of May and thereafter advective precipitation events prevail during the dry season. In the dry season, the coefficients R_A and M_R are considerably lower, except for October and November, which are the transition months to the rainy season. The maximum values of R_A are higher than 0.5 in the rainy season and generally lower than 0.5 in the dry season, with exception for the transition months. In addition, June shows a maximum R_A value over 0.5 and August close to 0.5, which can be explained by the high wind speeds during these months (Windhorst et al. 2013), making the advective moisture transport from the Amazon Basin most effective and provoking high precipitation amounts even in the valley of Loja during specific precipitation events.

The predominant wind direction was from the east during the entire months and for the whole study period (Table 2), which is due to the location of the study area in the tropical Andes of southern Ecuador (tropical easterlies). Therefore, most of the air masses, causing rainfall greater than 10 mm day^{-1}, came from the east. However, during the rainy season, most precipitation events with significant rainfall amounts came from the west (Table 2), making the proximity to the Pacific Ocean more important in this season. The highest precipitation was recorded between the months March and April, mainly originating from the northeast, although westerly flows brought considerable rainfall amounts (Tables 1, 2). In summary, the valley of Loja receives precipitation from the east and the west; from the Amazon Basin during the whole year, and additionally from the Pacific Ocean during the rainy season. During the transition month (April/May; October/November), the variability in wind direction is clearly observable (predominant paths; Table 1).

Figure 5 shows the dominant six storm pathways, representative for the selected 54 precipitation events analyzed. The underlying topographic map indicates that the storms mostly enter the valley through the natural course of the drainage systems, and therefore, stable blocked atmospheric conditions prevail. Only during periods of strong winds humidity enter directly from the east or the west, provoking the highest precipitation amounts at the upwind slopes of the barriers.

The moisture transport through the main river valley is impeded by the mountain barrier to the east and the west of the valley of Loja, reaching altitudes over 3000 m. However, the humidity enters trough depressions in the mountain ridges, depicted in Fig. 6, which shows the relief of the western barrier (profile 1; depressions: point A, 2600 m; point B, 2690 m; point C: 2750 m) and eastern barrier (profile 2;

Table 2 Summary of monthly storm parameter

Month	R_A		M_R	Season	Predominant path
	Minimum	Maximum			
December	0.00	0.53	32.31	Rainy	West
January	0.13	0.95	42.91	Rainy	West, east
February	0.13	0.66	48.23	Rainy	West
March	0.38	1.00	77.00	Rainy	Northeast
April	0.01	0.41	20.98	Rainy	Northeast
May	0.38	1.00	40.13	Dry	East
June	0.09	0.58	18.56	Dry	East
July	0.16	0.36	19.26	Dry	East
August	0.09	0.47	20.98	Dry	East
September	0.00	0.16	22.94	Dry	East
October	0.00	0.81	30.75	Dry	Southeast
November	0.05	0.61	36.30	Dry	Variable

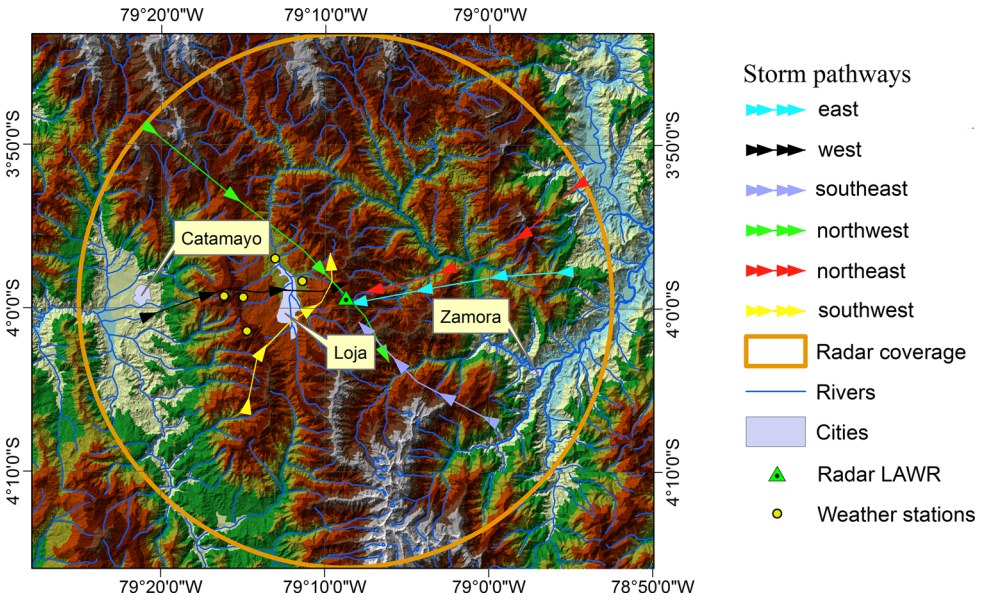

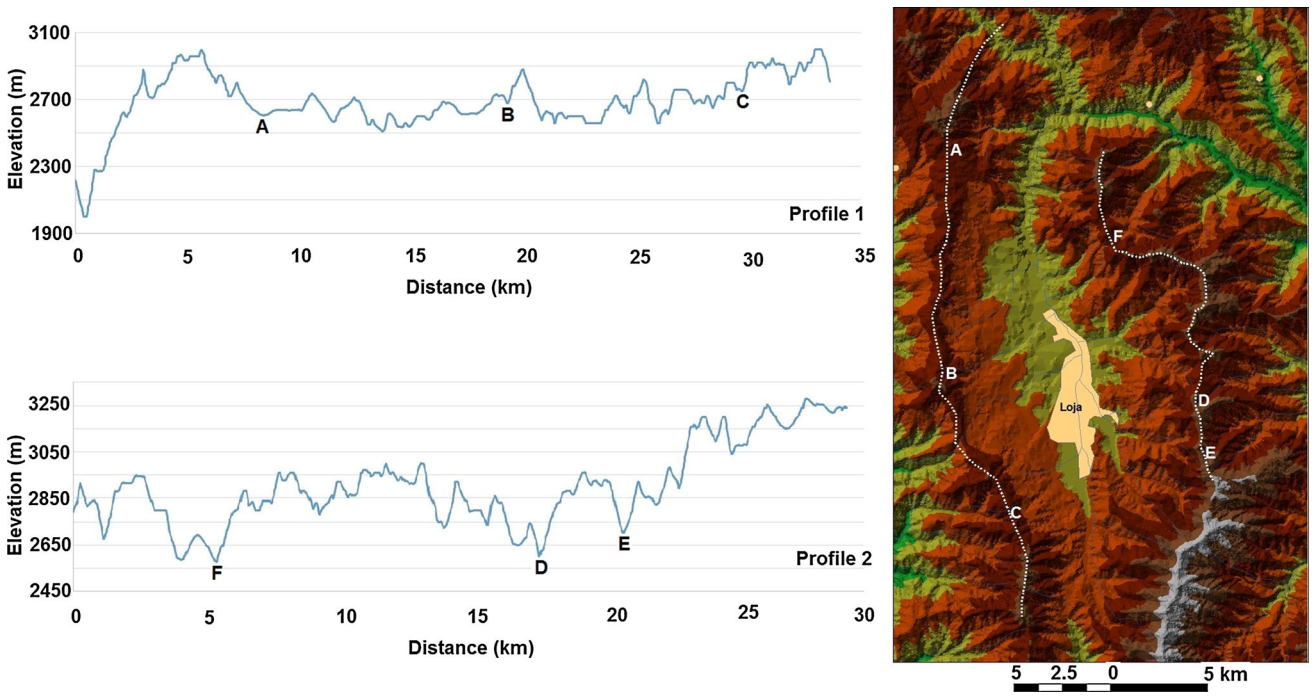

Fig. 5 Dominant storm trajectories

Fig. 6 Topographic profile of the western (*1*) and eastern (*2*) barrier in the valley of Loja

depressions: point D, 2600 m; point E, 2820 m; point F, 2575 m). These depressions are associated with canyons, formed by natural channels of the drainage network.

4 Conclusions

The LAWR radar data in combination with rain gauge measurements allowed the analyzation of the precipitation distribution in an Andean mountain valley in southern Ecuador, generating daily precipitation maps in high spatial resolution (100 m × 100 m). This resolution is able to detect the rainfall distribution even for smaller catchments and, therefore, can provide information for hydrological investigations. However, the accuracy of the precipitation maps depends on the density of the existing meteorological station network. Besides this, the identification of storm trajectories in combination with topographic data could identify the preferred storm pathways and their interaction with the

local relief, which can also help to improve Early Warning Systems (EWS).

The established R_A coefficient characterizes the magnitude of a storm, indicating the precipitation type and season. The R_A coefficient generally reaches values over 0.5 values during the rainy season (December to April), and values below 0.5 in the dry season (May to November). This trend showed some exceptions, notably the transition months, which illustrates the climatic variability within the study area. However, the highest rainfall amounts (M_R) were related to convective storms from the west, contributing to the major proportion of the precipitation totals during the rainy season.

Currently, two additional weather radars have been installed in southern Ecuador, forming, in conjunction with the LAWR, the first radar network in the tropical Andes (RadarNet-Sur; http://www.radarnetsur.gob.ec; Bendix et al. 2017). This prototype network will provide an important information for better understanding the evolution and distribution of regional precipitation as well as during ENSO (El Niño Southern Oscillation) events.

References

Barry RG (2008) Mountain weather and climate, 3rd edn. Cambridge University Press, Cambridge

Bell MM et al (2015) The Hawaiian Educational Radar Opportunity (HERO). Bull Am Meteorol Soc 96:2167–2181. doi:10.1175/BAMS-D-14-00126.1

Bendix J, Rollenbeck R, Palacios WE (2004) Cloud detection in the tropics-a suitable tool for climate ecological studies in the high mountains of Ecuador. Int J Remote Sensing 25:4521–4540

Bendix J, Trachte K, Cermak J, Rollenbeck R, Naub T (2009) Formation of convective clouds at the foothills of the tropical eastern Andes (South Ecuador). JAMC 48(8):1682–1695

Bendix J, Fries A, Zárate J, Trachte K, Rollenbeck R, Pucha-Cofrep F, Paladines R, Palacios I, Orellana J, Oñate-Valdivieso F, Naranjo C, Mendoza L, Mejia D, Guallpa M, Gordillo F, González-Jaramillo V, Dobbermann M, Celleri R, Carrillo C, Araque A, Achilles S (2017) RADARNET-SUR. Bull Am Meteorol Soc, FIRST RAIN RADAR NETWORK IN TROPICAL HIGH MOUNTAINS. doi:10.1175/BAMS-D-15-00178.1

Davis Instruments (2015) Wireless Vantage Pro2^{TM} and Vantage Pro2^{TM} Plus Stations, USA. http://www.davisnet.com/product_documents/weather/spec_sheets/6152_62_53_63_SS.pdf. Accessed 13 Jan 2016

Delrieu G, Wijbrans A, Boudevillain B, Faure D, Bonnifait L, Kirstetter PE (2014) Geostatistical radar-raingauge merging: a novel method for the quantification of the rain estimation accuracy. Adv Water Resour 71(2014):110–124. doi:10.1016/j.advwatres.2014.06.005

Ecuavisa (2015) Loja: Ocho casa se inundaron y sus propietarios evacuados. http://www.ecuavisa.com/articulo/noticias/nacional/103763-loja-8-casas-se-inundaron-sus-propietarios-evacuados. Accessed 01 Jan 2017

El Comercio (2015) Lluvias en Loja dejan seis fallecidos y viviendas inundadas. http://www.elcomercio.com/actualidad/lluvias-loja-fallecidos-sierranevada-invierno.html. Accessed 01 Jan 2017

Emck P (2007) A climatology of South Ecuador. Dissertation, Friedrich-Alexander Universität Erlangen, Germany

Espinoza JC, Chavez S, Ronchail J, Junquas C, Takahashi K, Lavado W (2015) Rainfall hotspots over the southern tropical Andes: spatial distribution, rainfall intensity, and relations with large-scale atmospheric circulation. Water Resour Res 51(5):3459–3475

Foresti L, Pozdnoukhov A (2012) Exploration of Alpine orographic precipitation patterns with radar image processing and clustering techniques. Meteorol Appl 19:407–419

Fries A, Rollenbeck R, Göttlicher D, Nauß T, Homeier J, Peters T, Bendix J (2009) Thermal structure of a megadiverse mountain ecosystem in southern Ecuador, and its regionalization. Erdkunde 63(4):321–335

Fries A, Rollenbeck R, Nauß T, Peters T, Bendix J (2012) Near surface air humidity in a megadiverse Andean mountain ecosystem in southern Ecuador and its regionalization. Agric For Met 152:17–30

Fries A, Rollenbeck R, Bayer F, Gonzalez V, Oñate-Valivieso F, Peters T, Bendix J (2014) Catchment precipitation processes in the San Francisco valley in southern Ecuador: combined approach using high-resolution radar images and in situ observations. Meteorol Atmos Phys 126:13–29

Gabella M, Notarpietro R (2004) Improving operational measurement of precipitation using radar in mountainous terrain—Part I: methods. IEEE Geosci Remote Sens Lett 1(2):78–83

Germann U, Joss J (2004) Operational measurement of precipitation in mountainous terrain. In: Meischner P (ed) Weather radar: principles and advanced applications. Springer, Berlin, pp 52–77

Germann U, Galli G, Boscacci M, Bolliger M (2006) Radar precipitation measurement in a mountainous region. Q J R Meteorol Soc 132(618):1669–1692

Germann U, Berenguer M, Sempere-Torres D, Zappa M (2009) REAL—ensemble radar precipitation estimation for hydrology in a mountainous region. QJR Meteorol Soc 135:445–456

Houze RA Jr, James CN, Medina S (2001) Radar observations of precipitation and airflow on the Mediterranean side of the Alps: Autumn 1998 and 1999. QJR Meteorol Soc 127:2537–2558

INAMHI (2009) Anuarios Meteorológicos. Quito, Ecuador. http://www.serviciometeorologico.gob.ec/biblioteca/. Accessed 01 Jan 2016

Jensen NE (2002) X-band local area weather radar—preliminary calibration results. Water Sci Technol 45:135–138

Jensen NE (2004) Local area weather radar documentation. DHI/LAWR/TN 2/10-2004. V 3.0, DHI Institute for the water environment

Jensen NE, Pedersen L (2005) Spatial variability of rainfall: Variations within a single radar pixel. Atmos Res 77:269–277

Johansson B, Chen D (2005) Estimation of areal precipitation for runoff modelling using wind data: a case study in Sweden. Clim Res 29:53–61

Krajewski WF, Kruger A, Smith JA, Lawrence R, Gunyon C, Goska R, Steiner M (2011) Towards better utilization of NEXRAD data in hydrology: an overview of Hydro-NEXRAD. J Hydroinform 13(2):255–266

Lengfeld K, Clemens M, Münster H, Ament F (2014) Performance of high-resolution X-band weather radar networks—the PATTERN example. Atmos Meas Tech 7:4151–4166

Ochoa-Cueva P, Fries A, Montesinos P, Rodríguez-Díaz JA, Boll J (2015) Spatial estimation of soil erosion risk by land-cover change in the Andes of southern Ecuador. Land Degrad Dev 26:565–573

Ochoa-Cueva P, Fries A, Mejia D, Burneo J, Ruíz-Sinoga J, Cerdà A (2016) Climate, landforms and soil erosion processes in a semiarid basin of the Ecuadorian Andes. CATENA 140:31–42

Panziera L, Germann U (2010) The relation between airflow and orographic precipitation on the southern side of the Alps as revealed by weather radar. QJR Meteorol Soc 136:222–238

Pedersen L, Jensen NE, Madsen H (2010) Calibration of local area weather radar—identifying significant factors affecting the calibration. Atmos Res 97(1–2):129–143

Richter M (2003) Using plant functional types and soil temperatures for eco-climatic interpretation in southern Ecuador. Erdkunde 57:161–181

Rollenbeck R, Bendix J (2006) Experimental calibration of a cost-effective X-band weather radar for climate ecological studies in southern Ecuador. Atmos Res 79(3–4):296–316

Rollenbeck R, Bendix J (2011) Rainfall distribution in the Andes of southern Ecuador derived from blending weather radar data and meteorological field observations. Atmos Res 99(2):277–289

Villarini G, Krajewski WF (2010) Review of the different sources of uncertainty in single polarization radar-based estimates of rainfall. Surv Geophys 31(1):107–129

Vuille M, Raymond S, Keimig B, Keimig F (2000) Interannual climate variability in the Central Andes and its relation to tropical Pacific and Atlantic forcing. J Geophys Res 105:12447–12460

Windhorst D, Waltz T, Timbe E, Frede HG, Breuer L (2013) Impact of elevation and weather patterns on the isotopic composition of precipitation in a tropical montane rainforest. Hydrol Earth Syst Sci 17:409–419